


Effect of Surface Ionic Screening on Polarization Reversal and Phase Diagrams in Thin Antiferroelectric Films for Information and Energy Storage

Anna N. Morozovska^{1,*}, Eugene A. Eliseev,² Arpan Biswas³, Nicholas V. Morozovsky,¹ and Sergei V. Kalinin^{3,†}

¹*Institute of Physics, National Academy of Sciences of Ukraine, pr. Nauky 46, 03028 Kyiv, Ukraine*

²*Institute for Problems of Materials Science, National Academy of Sciences of Ukraine, Krjijanovskogo 3, 03142 Kyiv, Ukraine*

³*Center for Nanophase Materials Sciences, Oak Ridge National Laboratory, Oak Ridge, Tennessee 37831, USA*

 (Received 25 June 2021; revised 11 September 2021; accepted 6 October 2021; published 27 October 2021)

Emergent behaviors in antiferroelectric thin films due to a coupling between surface electrochemistry and intrinsic polar instabilities are explored within the framework of the modified 2-4-6 Landau-Ginzburg-Devonshire (LGD) thermodynamic approach. By using phenomenological parameters of the LGD potential for a bulk antiferroelectric and a Stephenson-Highland (SH) approach, we study the role of surface ions with a charge density proportional to the relative partial oxygen pressure on the dipole states and their reversal mechanisms in antiferroelectric thin films. The combined LGDSH approach allows the boundaries of antiferroelectric, ferroelectriclike antiferroionic, and electretlike paraelectric states as a function of temperature, oxygen pressure, surface-ion formation energy and concentration, and film thickness to be delineated. This approach also allows the characterization of the polar and antipolar orderings dependence on the voltage applied to the antiferroelectric film, as well as the analysis of their static and dynamic hysteresis loops. The applications of the antiferroelectric films covered with a surface-ion layer for energy and information storage are explored and discussed.

DOI: [10.1103/PhysRevApplied.16.044053](https://doi.org/10.1103/PhysRevApplied.16.044053)

I. INTRODUCTION

Ferroelectric (FE) phase stability requires effective screening of the polarization bound charge at surfaces and interfaces with a nonzero normal component of polarization [1–3]. Rapid growth of FE thin-film applications in the 1990s necessitated the analysis of the microscopic mechanisms acting at ferroelectric interfaces, preponderantly effects stemming from nonzero spatial separation between spontaneous polarization and screening charges [4–8]. These effects are often introduced via the dead-layer [2] or physical-gap [9] concepts, postulating the presence of a thin nonferroelectric layer or gap separating the ferroelectric surface from the electrode. The validity of this approximation is confirmed by microscopic density-functional-theory studies [10–12].

However, the dead-layer approximation largely ignores the realistic details of the screening process at open surfaces and ferroelectric-semiconductor interfaces. In particular, stabilization of the FE state in ultrathin perovskite films can take place due to chemical screening (see, e.g., Refs. [13–15]), and screening via ionic

adsorption is intrinsically coupled to surface electrochemical processes [16–18]. This screening mechanism is confirmed by multiple experimental observations, including polarization retention above the Curie temperature [19], temperature-induced domain-potential inversion [20], formation of bubble domains during tip-induced switching [21–23], chaotic switching [7], and domain-shape instabilities [24]. Macroscopically, it is confirmed via chemical switching in ferroelectrics [13,25]. Finally, multiple anomalous observations, such as tip-pressure-induced switching [26,27] or continuous polarization states in ultrathin films, can be partially attributed to ionic screening [28]. This coupling results in a nontrivial influence on FE phase stability and phase diagrams [25,29], albeit the overall research efforts in this area are fairly small.

Early theoretical analyses, though studying the properties of ferroelectric materials in detail, typically ignore the nonlinear tunable characteristics of surface-screening charges. A complementary thermodynamic approach was developed by Stephenson and Highland (SH) [25,29], who considered an ultrathin film in equilibrium with a chemical environment that supplied (positive and negative) ionic species to compensate for polarization bound charges at the surface.

*anna.n.morozovska@gmail.com

†sergei2@ornl.gov

Recently, we modified the SH approach to allow for the presence of a gap between the ferroelectric surface covered by ions and a scanning probe microscope (SPM) tip [30–34] and developed an analytical description for the thermodynamics and kinetics of these systems. The analysis [30–34] leads to the elucidation of ferroionic states, which are the result of nonlinear electrostatic interactions between ions with a surface-charge density obeying the Langmuir adsorption isotherm and ferroelectric dipoles. The properties of these states are described by the system of coupled one-dimensional (1D) equations and corresponding phase diagrams are established.

Here, we study the role of surface ions with a charge density proportional to the partial oxygen pressure on the dipole states and the reversal mechanisms, as well as the corresponding phase diagrams of antiferroelectric (AFE) thin films. We use the SH approach combined with the 2-4-6 Landau-Ginzburg-Devonshire (LGD) thermodynamic potential to describe the polar and antipolar long-range orderings. It appears that, compared to FE materials, the considered AFE systems reveal more complex dynamics of polarization and surface charge due to presence of the FE-like antiferroionic (AFI) states. We analyze the corresponding phase diagrams and associated hysteresis loops, as well as the application of AFE films covered by a surface-ion layer for information and energy storage and multibit nonvolatile random access memory.

The manuscript is structured as follows. Section II contains the basic LGD equations and SH problem formulation with boundary conditions. Section III presents the free energy of the considered system. Numerical results (phase diagrams, hysteresis loops), discussion, and analysis are presented in Sec. IV. Section V is an outlook and brief summary. Parameters used in calculations and auxiliary figures are listed in the Supplemental Material [35].

II. BASIC EQUATIONS WITH BOUNDARY CONDITIONS

Here, we consider the system consisting of an electron-conducting bottom electrode, an AFE film, and a layer of surface ions with a charge density of $\sigma(\phi)$. An ultrathin gap of thickness $\lambda \sim 0.2 - 2$ nm separates the film surface and the top electrode, which is either an ion-conductive planar electrode or the flattened apex of the SPM tip. The gap provides direct ion exchange with an ambient medium, as shown in Fig. 1(a). In the case of perfect electric contact, $\lambda = 0$, ion exchange is impossible. A mathematical statement of the problem is listed in the Supplemental Material [35].

Due to the presence of an ultrathin dielectric gap between the top electrode and the surface of AFE film, the linear equation of state, $\mathbf{D} = \varepsilon_0 \varepsilon_d \mathbf{E}$, relates an electric displacement, \mathbf{D} , and field, \mathbf{E} , in the gap. Here, ε_0 is a

universal dielectric constant and $\varepsilon_d \sim 1 - 10$ is a relative permittivity in the gap filled by air with controllable oxygen pressure. A wide-band-gap AFE film can be considered as insulating, and here, $\mathbf{D} = \varepsilon_0 \mathbf{E} + \mathbf{P}$. The potential, ϕ , of a quasi-static electric field inside the film satisfies the Laplace equation in the gap and the Poisson equation in the film. The boundary conditions for the system are the equivalence of the electric potential to the applied voltage, U , at the top electrode (modeled by a flattened region, $z = \lambda$); the equivalence of the difference, $D_3^{\text{gap}} - D_3^{\text{film}}$, to the ionic surface charge density, $\sigma[\phi(\vec{r})]$, at $z = 0$; the continuity of ϕ at the gap-film interface, $z = 0$; and zero potential at the conducting bottom electrode, $z = h$ (see Fig. 1).

The polarization components of the uniaxial AFE film depend on the electric field, E_i , as $P_i = \varepsilon_0(\varepsilon_{ii}^f - 1)E_i$ and $P_3 = P_3^f + \varepsilon_0(\varepsilon_{33}^b - 1)E_3$, where ε_{ii}^f is the relative AFE dielectric permittivity; $i = 1, 2$; and ε_{33}^b is the relative antiferroelectric background permittivity, $\varepsilon_{33}^b \leq 10$ [36].

The polarization component, P_3^f , is further abbreviated as P_3 . To determine the spatial-temporal evolution of P_3 , one can use either the simplest two-sublattice Kittel model [37] or combine more complex models incorporating antipolar distortions related to oxygen-octahedra rotations in antiferrodistortive perovskites [38] (such as PbZrO_3) with the LGD approach. In fact, the seminal works of Haun *et al.* [39,40] do not follow the classical Kittel model. In the Kittel model, certain relationships exist between the expansion coefficients of the free energy in the polarization and antipolarization powers, whereas such relationships are not imposed in the Haun model. The topical review of Rabe [41], where earlier studies of antiferroelectrics are overviewed, concludes that available experimental facts about the AFE structure of complex oxides can be relatively well described by a simple Landau theory (e.g., Refs. [38,39]). In these theories, the antiferroelectric distortion is described by an order parameter that does not specifically require a two-sublattice character for the distortion.

Tagantsev *et al.* [42] suggest that a “missed” incommensurate phase exists in PbZrO_3 and that the transition to the AFE phase is driven by the softening of a single lattice mode via flexoelectric coupling. Later, Hlinka *et al.* [43] proposed a so-called trilinear coupling between antipolarization and oxygen-octahedra rotations as the source of antiferroelectricity in PbZrO_3 . The complex models [42,43] are promising for such an AFE as PbZrO_3 , but, at the same time, they can barely be included in the phenomenological LGD treatment.

Within the Kittel model, one can introduce the one-component polar and antipolar long-range-order parameters, $P = (1/2)[P_i^{(1)} + P_i^{(2)}]$ and $A = (1/2)[P_i^{(1)} - P_i^{(2)}]$, respectively, where $P_i^{(j)}$ is the i th component of the j th sublattice polarization. Within more complex models [38,39] the antiferroelectric distortion is described by

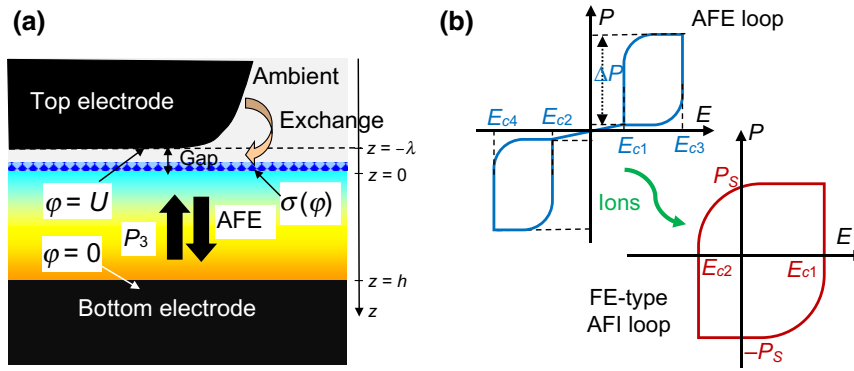


FIG. 1. (a) Layout of the considered system, consisting of an electron-conducting bottom electrode, an AFE film of thickness h , a layer of surface ions with charge density $\sigma(\phi)$, an ultrathin gap separating the film surface, and a top electrode (from bottom to the top). Film thickness is h ; gap thickness is λ . Adapted from Ref. [31]. (b) Schematics of the transition from an AFE-type polarization hysteresis to a FE-type AFI hysteresis loop induced by electric coupling with the charge of surface ions.

an order parameter that does not specifically require a two-sublattice character for the distortion.

Keeping the possible complexities in mind, we combine the above models with a 2-4-6-LGD thermodynamic potential for the description of long-range polar and antipolar orderings. At that, the nature of antipolar ordering is still controversial for many AFE perovskites, such as PbZrO_3 , and the classical Kittel, Haun, Whatmore, and Glazer models do not provide a complete quantitative description of their polar and structural properties, but it does not mean that the models are not applicable (at least semiquantitatively) to other AFEs.

Polarization rotation is only possible in multiaxial FEs and AFEs. For the film of a uniaxial AFE (or FE), the polar axis of which is normal to the film surfaces, only the “out-of-plane” components of the polar (P_3) and antipolar (A_3) long-range order define their polar properties (one-component approximation). For a single-domain state, which is stabilized by the electric field induced by oxygen ions (see, e.g., Refs. [13–15,25,29]), the properties weakly depend on the transverse coordinates, but can strongly vary with the distance, z , from the film surface (1D approximation). The validity of the one-component and 1D approximation used herein requires grounds.

An appropriate (as a rule, compressive) mismatch strain, caused by the difference between the film and substrate lattice constants, favors the stability of a “uniaxial” tetragonal phase with an out-of-plane polarization direction in thin epitaxial multiaxial perovskite films [44], which include PbZrO_3 . Hence, the application of an appropriate strain corroborates the validity of the one-component approximation. For a single-domain case, the mismatch strain leads to the renormalization of the coefficients in the LGD potential via the electrostriction coupling coefficients in a well-known way [see Eq. (3) in Ref. [44]]. On one hand, the coupling coefficients between the antipolar order parameter and strains are unknown. On the other hand, the circumstances allow us to assume that compressive strain (e.g., about 0.5% or higher) induces the tetragonal phase with an out-of-plane polarization in an AFE film, but the obtained results include a large uncertainty to be

quantitatively valid for a concrete perovskite, such as PbZrO_3 film.

Hence, the evolution and spatial distribution of the polar (P) and antipolar (A) order parameters are given by the coupled time-dependent 2-4-6 LGD equations:

$$\begin{aligned} \Gamma_P \frac{\partial P_3}{\partial t} + 2\alpha_p P + 4\beta_p P^3 + 2\chi P A^2 \\ + 6\gamma_p P^5 - g \frac{\partial^2 P}{\partial z^2} = E_3, \\ \Gamma_A \frac{\partial A}{\partial t} + 2\alpha_a A + 4\beta_a A^3 + 2\chi P^2 A + 6\gamma_a A^5 - g \frac{\partial^2 A}{\partial z^2} = 0. \end{aligned} \quad (1a)$$

Equation (1) follows from the variation of LGD free energy (see the Supplemental Material for details [35]). Here, $\Gamma_{P,A}$ are the positive kinetic coefficients defining the Khalatnikov relaxation of the order parameters. The coefficients $\alpha_p = \alpha_T(T_P - T)$ and $\alpha_a = \alpha_T(T_A - T)$ change their sign at the Curie temperature, T_P , and AFE temperature, T_A , respectively; T is the absolute temperature; and $\alpha_T > 0$. The inequalities $\gamma_a > 0$, $\gamma_p > 0$, and $g > 0$ should be valid for the LGD potential stability. The AFE-FE coupling coefficient, χ , should be positive for the stability of the AFE phase and negative for the stability of the FE phase. Let us underline that no other specific relationships are imposed on the coefficients in Eq. (1), expanding their applicability well beyond the oversimplified Kittel model.

The boundary conditions for P and A at the film surfaces, $z = 0$ and $z = h$, are of the third kind,

$$\left(P \mp \Lambda_P \frac{\partial P}{\partial z} \right) \Big|_{z=0,h} = 0 \quad \text{and} \quad \left(A \mp \Lambda_A \frac{\partial A}{\partial z} \right) \Big|_{z=0,h} = 0, \quad (1c)$$

and include extrapolation lengths, $\Lambda_{A,P}$ [45,46]. Notably, the value of the extrapolation length is a poorly known parameter in LGD phenomenology. It can vary by an order of magnitude due to the structure of the surface or interface. In particular, Ref. [46] gives $\Lambda_P = 2$ nm for the perovskite $\text{SrRuO}_3/\text{PZT}$ (PZT, lead zirconate titanate)

interface, while for the other film surface the parameter Λ_P is close to zero. For the ferroelectric-electrochemically active ambient medium, the values of extrapolation length can differ strongly from the case of the interface between two perovskites. We do not find any reliable data for the Λ_A value calculated or measured for AFE surfaces. For typical perovskite parameters, the boundary conditions of Eq. (1c) determine the behavior of polarization and antipolarization in the layer with a thickness not more than several correlation lengths in the z direction, $L_z^C \cong \sqrt{\epsilon_0 \epsilon_{33}^b g} < 0.5$ nm, which is much smaller than the temperature-dependent correlation length in the x direction, $L_x^C \cong \sqrt{(g/|\alpha_p|)} \sim (1 - -5)$ nm, due to the presence of the depolarization field in the z direction and its practical absence in the x direction for a single-domain state. So, the scale of the out-of-plane polarization variation related to the extrapolation length effect is typically smaller than the lattice constant [47]. Allowing for the applicability of the LGD approach for a length scale significantly higher than the lattice constant, the short-range effects related to the extrapolation length can be neglected.

An equation for the surface charge is analogous to the Langmuir adsorption isotherm used in interfacial electrochemistry for adsorption on a conducting electrode exposed to ions in a solution [48]. To describe the dynamics of surface-ion charge density, we use a linear relaxation model,

$$\tau \frac{\partial \sigma}{\partial t} + \sigma = \sigma_0(\phi), \quad (2)$$

where the dependence of an equilibrium surface-charge density, $\sigma_0(\phi)$, on the electric potential, ϕ , is controlled by the concentration of surface ions, $\theta_i(\phi)$, at the interface, $z = 0$, in a self-consistent manner, as proposed by Stephenson and Highland [25,29]:

$$\sigma_0[\phi] = \sum_{i=1,2} e Z_i N_i \theta_i(\phi) \equiv \sum_{i=1,2} e Z_i N_i \times \left[1 + \rho^{1/n_i} \exp \left(\frac{\Delta G_i^{00} + e Z_i \phi}{k_B T} \right) \right]^{-1}, \quad (3)$$

where e is an elementary charge, Z_i is the ionization degree of the surface ions, and N_i are the saturation densities of the surface ions. Subscript i designates the summation of positive ($i = 1$) and negative ($i = 2$) charges; $\rho = (p_{O_2}/p_{O_2}^{00})$ is the relative partial pressure of oxygen (or other ambient gas) introduced in Ref. [25], and n_i is the number of surface ions created per gas molecule. Two surface charge species exist, since the gas molecule is electroneutral before its electrochemical decomposition starts. The dimensionless ratio ρ varies over a wide range from 10^{-6} to 10^6 in the SH approach [25,29].

Positive parameters ΔG_1^{00} and ΔG_2^{00} are the free energies of surface-defect formation under normal conditions,

$p_{O_2} = p_{O_2}^{00}$, while the latter is set to equal 1 bar, and zero applied voltage, $U = 0$. The energies ΔG_i^{00} are responsible for the formation of different surface charge states (ions, vacancies, or their complexes). Specifically, exact values of ΔG_i^{00} are poorly known, even for many practically important cases, and so hereafter they are regarded to vary in the range over about 0.1 to 1 eV [25]. At that the difference, $\Delta G_1^{00} - \Delta G_2^{00}$ can play a crucial role in the overall behavior of a ferroelectric film covered by ions [25]. Notably, the developed solutions are insensitive to the specific details of the charge-compensation process [49] but are sensitive to the thermodynamic parameters of corresponding reactions [50].

III. FREE ENERGY OF THE ANTIFERROIONIC SYSTEM AND CALCULATION DETAILS

A. Free energy of the antiferroionic system

The stabilization of single-domain polarization in ultra-thin FE perovskite films takes place due to chemical switching (see, e.g., Refs. [13–15,25,29]), because the built-in field induced by the surface ionic charge is relatively high, even when the relative oxygen pressure, ρ , deviates from the equilibrium value, $\rho = 1$, not very strongly (e.g., for $10^{-2} \leq \rho \ll 10^{-2}$), and the high field supports the out-of-plane orientation of polarization [30–34]. The domain structure is absent in the AFE phase of the film, but it may appear in the FE-like state due to the presence of the gap (i.e., for $\lambda > 0$). However, as shown below, the FE-like state can be induced by a strong oxygen excess or deficiency (e.g., for $\rho \ll 10^{-2}$). As a rule, a single-domain configuration is stable in the case of $\rho \ll 1$ (or $\rho \gg 1$) because both factors, the built-in field and the screening degree produced by the oxygen ions, are high enough to support the unipolar orientation of polarization. Since both factors are present in the considered case, and the gap width is typically very small, i.e., $(\lambda/h) \ll 1$, a single-domain approximation can be used hereafter.

Thus, we will assume that the distributions of $P(x, y, z)$ and $A(x, y, z)$ do not deviate significantly from their values, averaged over the film thickness, which are further abbreviated as “polarization” $P \cong \langle P \rangle$ and “antipolarization” $A \cong \langle A \rangle$. In this case, the behavior of P and A , and surface charge density, σ , can be described via nonlinear coupled algebraic equations, similar to the ones derived in Refs. [30–34] for P and σ .

Below, we consider either the stationary case or adiabatic conditions, when $\sigma = \sigma_{of}$. The expression for the free-energy density per unit area, f , the minimization of which gives coupled equations for polarization dynamics, is the sum of the LGD polar and antipolar ordering energy, f_{AP} , and the electrostatic energy f_ψ . f_ψ includes the polarization interaction energy with overpotential Ψ ; the energy of the electric field in the AFE film and the energy in the

gap, correspondingly; and the surface charge energy. So $f = f_{AP} + f_{\Psi}$, and the individual contributions are

$$f_{AP} = h[\alpha_p P^2 + \alpha_a A^2 + \chi P^2 A^2 + \beta_p P^4 + \beta_a A^4 + \gamma_p P^6 + \gamma_a A^6], \quad (4a)$$

$$f_{\Psi} = -\Psi P - \varepsilon_0 \varepsilon_{33}^b \frac{\Psi^2}{2h} - \frac{\varepsilon_0 \varepsilon_d (\Psi - U)^2}{2\lambda} + \int_0^{\Psi} \sigma_0[\varphi] d\varphi. \quad (4b)$$

Here, $\alpha_p = \alpha_{pT}(T - T_p) + (2g/h\Lambda_p)$ and $\alpha_a = \alpha_{aT}(T - T_a) + (2g/h\Lambda_a)$ are the thickness-dependent and temperature-dependent functions. The terms g/h originate from ‘‘intrinsic’’ gradient-correlation size effects. The voltage U is applied between the electrodes.

The free energy given by Eq. (4) has an absolute minimum at high Ψ . According to the Biot variational principle [51], we can further use a thermodynamic potential, the partial minimization of which over P will give the coupled equations of state, and, at the same time, it has an absolute minimum at finite P values.

B. Calculation details

So, a formal minimization of Eq. (4), $(\partial f / \partial P) = -\Gamma_P(\partial P / \partial t)$, $(\partial f / \partial A) = -\Gamma_A(\partial A / \partial t)$, and $(\partial f / \partial \Psi) = 0$ leads to coupled time-dependent relaxation-type differential equations for the polarization, antipolarization, and overpotential:

$$\Gamma_P \frac{\partial P}{\partial t} + 2(\alpha_p + \chi A^2)P + 4\beta_p P^3 + 6\gamma_p P^5 = \frac{\Psi}{h}, \quad (5a)$$

$$\Gamma_A \frac{\partial A}{\partial t} + 2(\alpha_a + \chi P^2)A + 4\beta_a A^3 + 6\gamma_a A^5 = 0, \quad (5b)$$

$$\frac{\Psi}{h} = \frac{\lambda(\sigma_0 - P) + \varepsilon_0 \varepsilon_d U}{\varepsilon_0(\varepsilon_d h + \lambda \varepsilon_{33}^b)}. \quad (5c)$$

The overpotential, Ψ , contains the contribution from surface charges proportional to σ_0 , the depolarization field contribution proportional to P , and the external potential drop proportional to U .

Equation (5) is solved numerically and the obtained stationary solutions are substituted into the energy of Eq. (4) to determine the energy of the corresponding state. Since Eq. (5b) is homogeneous, one can find the static solutions for A , namely, $A = 0$ or

$$A^2 = \frac{2\beta_a \pm \sqrt{\beta_a^2 - 12\gamma_a(\alpha_a + \chi)P^2}}{6\gamma_a},$$

and substitute them into Eq. (5a). Further substitution of the overpotential, Ψ [as a function of $\sigma_0(U)$, P , and U] from Eq. (5c) into Eq. (5a) allows us to plot the parametric dependence, $U(P)$, the inverse of which gives us the static $P(U)$ and $A(U)$ dependences.

The LGD thermodynamic potential can be further expanded in A , P , and Ψ powers, assuming that $|eZ_i \Psi / k_B T| \ll 1$ (see the Supplemental Material [35] for details). As a result, we obtain the expression for free energy:

$$F[P, A] = \alpha_{pR} P^2 + \beta_{pR} P^4 + \gamma_{pR} P^6 - (E_{SI} + E_{act})P + \chi_R P^2 A^2 + \alpha_a A^2 + \beta_a A^4 + \gamma_a A^6. \quad (6)$$

Renormalized coefficients, α_{pR} , β_{pR} , γ_{pR} , and χ_R , built-in field E_{SI} , and acting field E_{act} are

$$\alpha_{pR}(T, \rho, h) = \alpha_p [1 + S(T, \rho, h)] + \frac{\lambda}{2\varepsilon_0(\varepsilon_d h + \lambda \varepsilon_{33}^b)}, \quad (7a)$$

$$\begin{aligned} \beta_{pR}(T, \rho, h) &= [1 + S(T, \rho, h)]\beta_p, \quad \gamma_{pR}(T, \rho, h) \\ &= [1 + S(T, \rho, h)]\gamma_p, \end{aligned} \quad (7b)$$

$$\chi_R(T, \rho, h) = [1 + S(T, \rho, h)]\chi, \quad (7c)$$

$$\begin{aligned} E_{SI}(T, \rho, h) &= \frac{\lambda}{\varepsilon_0(\varepsilon_d h + \lambda \varepsilon_{33}^b)} \sum_{i=1,2} eZ_i N_i f_i(T, \rho), \quad E_{act}(U, h) \\ &= -\frac{\varepsilon_d U}{\varepsilon_d h + \lambda \varepsilon_{33}^b}. \end{aligned} \quad (7d)$$

The first term in Eq. (7a), $\alpha_p [1 + S(T, \rho, h)]$, is renormalized by the influence of the surface charge caused by the adsorption-desorption of oxygen ions via the function $S(T, \rho, h)$. The last term in Eq. (7a), $\lambda / [2\varepsilon_0(\varepsilon_d h + \lambda \varepsilon_{33}^b)]$, originates from the depolarization field. The first expression in Eq. (7d) is the built-in electric field created by surface ions, $E_{SI}(T, \rho, h)$, which is significant for thin films being proportional to the ratio λ/h . Since, as a rule, $\varepsilon_d h \gg \lambda \varepsilon_{33}^b$, the acting field is close to an external field, $E_{act} \approx -(U/h)$. Also, we introduce positive functions in Eq. (7):

$$\begin{aligned} S(T, \rho, h) &= \frac{\lambda h}{\varepsilon_0(\varepsilon_d h + \lambda \varepsilon_{33}^b)} \sum_{i=1,2} N_i \frac{[eZ_i f_i(T, \rho)]^2}{k_B T}, \quad f_i(T, \rho) \\ &= \left[1 + \rho^{1/n_i} \exp\left(\frac{\Delta G_i^{00}}{k_B T}\right) \right]^{-1}. \end{aligned} \quad (7e)$$

It is seen from Eq. (7) that the influence of the relative partial oxygen pressure on the AFE thin film reduces the influence of the surface charge, $\sigma_0(\phi)$, caused by the adsorption-desorption of oxygen ions. The influence is introduced via the positive function $S(T, \rho, h)$ and the built-in electric field, $E_{SI}(T, \rho, h)$, penetrating the entire the depth of the film. Since $(\Delta G_i^{00} / k_B T) > 3$ for $\Delta G_i^{00} \geq 0.2$ eV and $|T| < 500$ K, $\exp(\Delta G_i^{00} / k_B T) \gg 1$ over the actual temperature range, $|T| < 500$ K. Thus, the function $S(T, \rho, h)$ rapidly grow for high ($\rho \gg 1$) and low ($\rho \ll 1$)

pressures, and thus, it can significantly increase the absolute value of the negative coefficient, $\alpha_p[1 + S(T, \rho, h)]$. As a result, the coefficient $\alpha_{pR}(T, \rho, h)$ can become more negative than α_a , opening up the possibility of the FE phase's emergence at high excess ($\rho \gg 1$) and deficient ($\rho \ll 1$) relative partial pressures. Below, we will show and analyze the possibility. Experimental evidence of this effect in FE films is given in Refs. [13–15,25,29]. This work states that the same mechanism of FE-phase induction by oxygen exposure-deficiency should exist in AFE films, but it is unlikely to be noticeable in the bulk AFE, because Eq. (7) is only valid for thin films.

1. The case of the second-order phase transition (2-4 Landau expansion)

Notably, in the case of the AFE film with second-order phase transitions, when $\beta_{a,p} > 0$ and $\gamma_{a,p} = 0$, analytical solutions for the phase energy, order parameters, and critical (or coercive) fields of double- (or single-) hysteresis loops are possible after a trivial minimization of the Landau energy, Eq. (6). They are summarized in Table I. The boundaries between the AFE phase, mixed ferrielectric FEI phase, pressure-induced FE-like AFI phase, and paraelectric phase correspond to the condition of the phase-energy equality. Below, we are specifically interested in the pressure-induced transition from the AFE phase to the FE-like AFI phase. The FE-like AFI phase becomes absolutely stable if $\alpha_{pR} < 0$ and $F_{AFI} < 0$ is minimal in comparison with F_{AFE} and F_{FEI} . When $\alpha_a > 0$ at $T > T_A$ and we use $\chi < 0$ for the AFE phase's stability, the following condition is sufficient for the absolute stability of the AFI phase:

$$\alpha_{pR}(T_A, \rho, h) \leq 0. \quad (8)$$

We use a Gaussian process model (GPM) for rapid exploration and prediction of phase diagrams and order

parameters corresponding to the free energy, Eq. (6), for the case of $\beta_{a,p} > 0$ and $\gamma_{a,p} = 0$ in the Supplemental Material[35]. The material parameters are listed in Table D1 and the results are shown in Figs. D1–D4 [35]. In the GPM-predicted image, we can see similar distinctive regions with different color coding, and thus, giving us the interpretation of individual phases. We can have a better prediction of phases with more advanced acquisition functions (exploration-exploitation) to sample with respect to user criteria (for example, we can conduct adaptive sampling, where the objective function is higher). We observe that, as ρ increases or decreases by an order of 10 for temperature $T < T_p$, we are approaching a FEI phase where, with further increases or decreases of ρ by an order of 10, deeper wells for order parameter A are shifted to deeper wells for order parameter P . Also, as the parameters h and ΔG_i^{00} decrease, the FEI region shrinks and expands, respectively, for the same parameter space of T, ρ . As defined in Table I, we do not find the AFI region ($A = 0, P_S \neq 0$) in Figs. D1–D4; the codes are available in Ref. [35].

2. The case of the first-order phase transition (2-4-6 Landau expansion)

For an illustration of the numerical results, we use an AFE film with thickness $h = 5 - 50$ nm separated from the tip electrode by a gap of thickness $\lambda = 0 - 2$ nm. Also, we regard that the ion-formation energies are equal under normal conditions and small, $\Delta G_1^{00} = \Delta G_2^{00} = 0.2$ eV. Using the results of Haun *et al.* [39,40], we determine the LGD expansion coefficients for a model antiferroelectric, PbZrO₃ (see the Supplemental Material [35]). It appears that $\beta_{a,p} < 0$ and $\gamma_{a,p} > 0$ for this material, and thus, the 2-4-6 LGD expansion must be used. Corresponding expansion coefficients and other parameters are listed in Table C1 within the Supplemental Material [35].

TABLE I. Thermodynamic phases, order parameters, energy, and critical fields calculated for $\beta_{a,p} > 0$ and $\gamma_{a,p} = 0$.

Phase	Order parameters at $E_{\text{act}} = -E_{\text{SI}}$	Free energy at $E_{\text{act}} = -E_{\text{SI}}$	Critical field(s) E_c
AFE	$A_S = \pm \sqrt{-\alpha_a/2\beta_a} P_S = 0$ $\Delta P \cong \pm \sqrt{-\frac{\alpha_{pR}}{6\beta_{pR}}}$ [see Fig. 1(b) for definitions]	$F_{\text{AFE}} = -\frac{\alpha_a^2}{4\beta_a},$ $\alpha_a < 0$	$E_{c1,2} = \frac{\pm 1}{3\sqrt{3}} \frac{(-\alpha_{pR} + \frac{\chi R \alpha_a}{2\beta_a})^{3/2}}{\beta_{pR} - \frac{\chi R^2}{4\beta_a}} - E_{\text{SI}}$ $E_{c3,4} = \pm \frac{1}{3\sqrt{3}} \frac{(-\alpha_{pR})^{3/2}}{\beta_{pR}} - E_{\text{SI}}$
FEI	$P_S = \pm \sqrt{\frac{2\alpha_{pR}\beta_a - \chi R \alpha_a}{4\beta_a\beta_{pR} - \chi R^2}}$ $A_S = \pm \sqrt{\frac{2\alpha_a\beta_{pR} - \chi R \alpha_{pR}}{4\beta_a\beta_{pR} - \chi R^2}}$	$F_{\text{FEI}} = -\frac{\alpha_a^2\beta_{pR} + \alpha_{pR}^2\beta_a - \chi R \alpha_a \alpha_{pR}}{4\beta_a\beta_{pR} - \chi R^2}$	$E_{c1,2} = \frac{\pm 1}{3\sqrt{3}} \frac{(-\alpha_{pR} + \frac{\chi R \alpha_a}{2\beta_a})^{3/2}}{\beta_{pR} - \frac{\chi R^2}{4\beta_a}} - E_{\text{SI}}$
FE-like AFI	$P_S = \pm \sqrt{-\frac{\alpha_{pR}}{2\beta_{pR}}}$ $A_S = 0$	$F_{\text{AFI}} = -\frac{\alpha_{pR}^2}{4\beta_{pR}},$ $\alpha_{pR} < 0$	$E_{c1,2} = \pm \frac{1}{3\sqrt{3}} \frac{(-\alpha_{pR})^{3/2}}{\beta_{pR}} - E_{\text{SI}}$
PE	$A_S = P_S = 0$	0	absent

However, the coefficients from Table C1 [35] do not capture all important features of a bulk PbZrO_3 , as we note several discrepancies in the temperature behavior of the calculated and measured critical fields and polarization hysteresis shape [52–55]. We relate the discrepancy with the strong influence of an antiferrodistorsive subsystem (oxygen-octahedra tilt) that is missed in the Kittel model and underestimated in the Haun model. A complete and self-consistent phenomenological description of PbZrO_3 in terms of antiferroelectric and electrocaloric properties [56] and anomalous ferroelectricity [42], allowing for antiferrodistortion [38,41,43], is an important problem beyond the scope of this work. However, the ferroelectricity observed in thin PbZrO_3 films [57] is within the scope of our work, at least partially.

When calculating the hysteresis loops of polarization, $P(U)$, at nonzero frequency, ω , of the applied voltage, $U = U_0 \sin(\omega t)$, we use different kinetic coefficients, $\Gamma_P \gg \Gamma_A$, to make the characteristic relaxation time of P much longer than the relaxation time of A . The strong inequality of $\Gamma_P \gg \Gamma_A$ leads to polarization relaxation with a characteristic time of $\tau = (\Gamma_P/2|\alpha_p|)$, while antipolarization behaves adiabatically. Hence, the dimensionless frequency, $w = \omega\tau$, governs the polarization response to an external field.

To avoid “sticking” of the system at local minima, we apply a very small fictitious “antifield” (with an amplitude smaller than 10^{-6} V/nm) acting on the antipolarization, A . The physical origin of the antifield is related to variations of the local electric field. The calculations are performed and visualized in MATHEMATICA 12.2 ©Wolfram Research software [35].

IV. RESULTS

A. Phase diagram, free-energy relief, and hysteresis loops of a thick antiferroelectric film without surface ions

The phase diagram of a very thick AFE film as a function of temperature is shown in Fig. 2(a). Here, the surface ions from ambient media are absent and the gap is either absent or very small, such that the film approaches bulk conditions. In accordance with available experimental results [38–43], the diagram contains the region of an AFE phase followed by an AFE phase coexisting with a “weak” FE phase and then a paraelectric (PE) phase. The first-order phase transition between the AFE and PE phases occurs at $T_A \cong 490$ K, and the boundary between the AFE and AFE-FE phases is very diffuse and located at around $T_P \cong 460$ K.

Contour maps of the free energy dependence on polarization and antipolarization are shown in the upper insets of Fig. 2(b)–(d) for different temperatures, $T = 200, 450$, and 500 K, and zero field, $E = 0$. There are two relatively deep A wells ($A = \pm A_S, P = 0$) and two very shallow

P wells ($P = \pm P_S, A = 0$) in the “deep” AFE phase at $T \ll T_P < T_A$ [inset (b) for 200 K]. Both A wells have the same depth, and both P wells have the same depth. The A wells and P wells are separated by four saddle points. The A wells become significantly shallower when the temperature approaches T_P [compare the minimal-energy value (-7.2 rel. units) in the inset of Fig. 2(c) for 450 K with -75 rel. units in the inset of Fig. 2(b) for 200 K]. At temperatures $T_P \leq T < T_A$, all wells still have negative energy, but the relative difference between the depth of A wells and P wells is much smaller than that at $T \ll T_P$, indicating that the temperature range corresponds to coexisting stable polar and antipolar states. The well energies become positive and so polar and antipolar states become metastable at $T > T_A$ [inset of Fig. 2(d) for 500 K]. Then, the wells disappear completely in the deep PE phase at $T \gg T_A$.

The relief of the free energy determines the temperature behavior of polarization dependence on the external E field, $P(E)$, where $E = (U/h)$. The quasi-static dependence of $P(E)$ is mostly hysteretic, and its shape gradually changes from a double-antiferroelectric-type loop to a loop with a thin constriction, and then to a paraelectriclike curve as the temperature increases from 200 to 500 K [see dark-red and red curves in the insets of Fig. 2(e)–(g)]. However, the transition from the red curves to dark-red curves takes place only when $E > E_c$, where E_c is the static critical field. The dependence of $P(E)$ is quasi-linear at $E < E_c$ [see red parts of the $P(E)$ curves]. Notably, the $P(E)$ curves are antisymmetric with respect to the E axis, since the built-in field, E_{SI} , is absent due to the absence of surface ions.

Polarization hysteresis loops, $P(E)$, calculated for low dimensionless frequencies, $w \ll 1$, almost coincide with the static P curves [compare black loops in plots (h)–(j) with red curves in plots (e)–(g) in Fig. 2]. The frequency increase in the range $1 \leq w \leq 3$, which leads to the appearance of a thin constriction between the double loops in the AFE phase, as well as to the loop opening in the PE phase [see red loops in plots (h)–(j) in Fig. 2]. The width of the constriction increases significantly with a further increase of w , and the loop acquires a ferrielectriclike shape in the AFE phase [see magenta, blue, and green loops in plot (h) in Fig. 2]. At the same time, the frequency increase ($3 \leq w \leq 10$) at higher temperatures leads to an opening of a ferroelectriclike loop, meaning that the opening is a purely dynamic effect [see magenta, blue, and green loops in plot (i) in Fig. 2]. The dynamic effect allows us to classify the temperature region as an AFE-FE coexisting region. High frequency, $w \geq 10$, opens a pseudo-ferroelectric loop, even in the PE phase [see magenta, blue, and green loops in plot (j) in Fig. 2].

Notably, the phase set (AFE, AFE-FE, and PE) calculated within the 2-4-6 Landau expansion with material parameters from Table C1 [35] and shown in Fig. 2(a) differs from the analogous set (AFE, FEI, PE) calculated

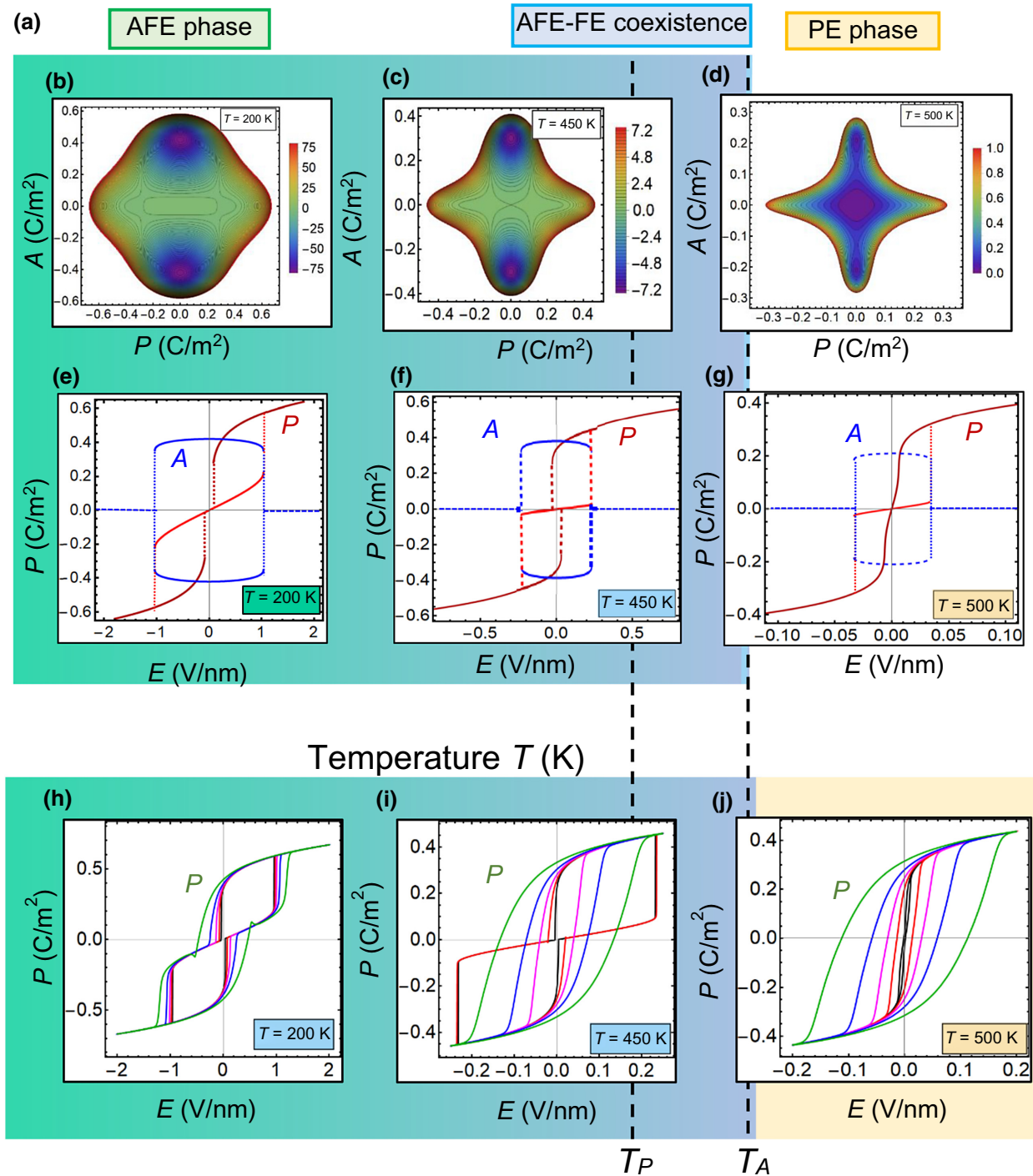


FIG. 2. Phase diagram of an AFE film (a). Contour maps of the free-energy dependence on polarization (P) and antipolarization (A) for temperature values of $T = 200$ (b), 450 (c), and 500 K (d), and $E = 0$. Relative units are used for the energy color scale. Dependences of A (dashed and dotted blue loops) and P (dashed red and dark-red loops) on the static external electric field, E , calculated for $T = 200$ (e), 450 (f), and 500 K (g). Polarization hysteresis, $P(E)$, calculated for dimensionless frequencies $\omega = 0.3$ (black loops), 3 (red loops), 10 (magenta loops), 30 (blue loops), and 100 (green loops), and temperatures $T = 200$ (h), 450 (i), and 500 K (j). For plots (h)–(j), external electric field is $E = (U_0/h) \sin(\omega t)$ and dimensionless frequency is $\omega = (\omega \Gamma_P / 2 |\alpha_P|)$. surface charges from ambient medium are absent. Gap thickness, $\lambda < 0.1$ nm; film thickness, $h > 500$ nm. Other parameters are listed in Table C1 [35].

within the 2-4 Landau expansion with material parameters from Table D1 and shown in Figs. D1–D4 [35]. Since $\beta_{a,p} > 0$ and $\gamma_{a,p} = 0$ and $\beta_{a,p} < 0$ and $\gamma_{a,p} > 0$ for the 2-4 and 2-4-6 Landau expansions, respectively, as well as the effect of ρ is not considered in Fig. 2(a), the difference in the phase set seems natural.

Comparing the diagram in Fig. 2(a) with well-known literature data [38–43], we conclude that our model with parameters from Table C1 [35] describes correctly all the main experimental features of the phase transitions in PbZrO_3 , namely, the sequence of phases: AFE phase \rightarrow AFE-FE coexistence \rightarrow PE-like state. Also, the experimentally observed transition from a double-antiferroelectriclike hysteresis loop to a constricted ferroelectriclike loop and then to a PE-like dynamic loop with increasing temperature is correctly reproduced in Figs. 2(h)–2(j). However, the model does not describe several minor features of the hysteresis loops observed in some (but not all) experiments, such as the “stretched” constriction and AFE loops separated by a long linear region [such as that shown in Fig. 1(b)]. It also does not reproduce correctly the temperature behavior of the critical fields.

The next question is what will change in Fig. 2 if bulk PbZrO_3 is placed in an oxygen environment. In our model, the bulk is achieved by considering a very thick PbZrO_3 film with one (or both) surface exposed to oxygen pressure. It appears that the effect of the partial oxygen pressure is significant only in the immediate vicinity of the film surface, since the depolarization field, the built-in electric field induced by ions, and the renormalization of the free-energy coefficients are proportional to the ratio of the gap width, λ , to the film thickness, h . Therefore, the consideration of a very thick film with $h \gg 10^{-3}\lambda$ leads to results that are barely distinguishable from those shown in Fig. 2.

B. The influence of surface ions on the phase diagram, free-energy relief, and hysteresis loops of antiferroelectric films

The free energy as functions of polarization (P) and antipolarization (A) calculated for several temperatures (T) and relative partial oxygen pressures (ρ), that values of which are listed for each column or row, are shown in Fig. 3. There are two very deep A wells ($A = \pm A_S, P = 0$) and two very shallow P wells ($P = \pm P_S, A = 0$) in the deep AFE phase at temperatures well below $T_P \approx 460$ K and $10^{-6} < \rho < 10^4$ [see columns (a)–(c) for 200–400 K]; the wells become shallower at $T \rightarrow T_A$ and eventually disappear as the temperature increases well above $T_A \approx 490$ K [see column (d) for 500 K]. Both A wells have the same depth independent of the values of ρ and T . The relative depth of the P wells depends on the ρ and T values. The right well ($P = +P_S$) is evidently deeper for $\rho \gg 1$ and $T > T_A$; they are almost equal for $10^{-4} < \rho < 10^4$ and $T < 400$ K, and exactly equal for $\rho = 1$ independent of

T ; the left well ($P = -P_S$) becomes evidently deeper for $\rho \ll 1$ and $T > T_A$ (compare the top, middle, and bottom rows). The origin of the P -well asymmetry is the built-in electric field, E_{SI} , induced by the surface-ion charge. This field is approximately proportional to the difference ($\rho^{1/n_i} - \rho^{-1/n_i}$), and thus, the magnitude of E_{SI} increases with the deviation of ρ from unity, and the sign of E_{SI} changes when $\rho \rightarrow (1/\rho)$, which is a direct consequence of Eqs. (7d) and (7e) at $\Delta G_1^{00} = \Delta G_2^{00}$. The sign change of E_{SI} explains the left (or right) asymmetry of the P wells.

The A wells and P wells are separated by four saddle points. At temperatures lower than T_A , both A wells and P wells have negative energy, i.e., they correspond to stable polar and antipolar states. The energy of the A wells becomes positive and the corresponding states become metastable at $T > T_A$ [see column (d) for 500 K]. The A wells disappear at $T \gg T_A$. Both P wells acquire positive energy at $T > T_P$ and disappear at $T \gg T_A$ only when $10^{-2} < \rho < 10^2$. Either right or left negative wells appear when $\rho > 10^2$ or $\rho < 10^{-2}$, respectively. This means that the built-in electric field, E_{SI} , induced by the surface-ion charge creates and supports a FE-like AFI state, which is characterized by the asymmetric potential relief, and the asymmetry increases with excess ($\rho \gg 1$) or a deficiency ($\rho \ll 1$) of oxygen ions at the film surface [see Eq. (7d) for details].

Since the case of $\rho \gg 1$, corresponding to high oxygen excess, is hard to realize in practice, below we mainly discuss the easier-to-realize case of oxygen deficiency, $\rho \leq 1$, keeping in mind that the physical picture at $\rho \geq 1$ differs the one at $\rho \leq 1$ only by asymmetry with respect to the P axis of the potential relief (the left or right well is deeper), since corresponding built-in fields lead to left or right shifts of polarization loops and curves, respectively.

The dependences of A (blue curves) and P (red and dark-red curves) on the static electric field, E , are shown in Fig. 4 for $T = 200 - 500$ K (columns a–d) and relative oxygen pressures of $\rho = 1, 10^{-4}$, and 10^{-6} (from top to bottom rows, respectively), the values of which are listed for each column or row. The red and dark-red polarization curves are two nonzero stable solutions of Eq. (5a). Dotted vertical lines show the thermodynamic transitions between different polar and antipolar states.

Changes, which occur with the shape of the loops in vertical columns (a)–(d), with the increase in temperature, mainly consist of a decrease in the width and height of A and P loops, and the appearance of a noticeable asymmetry of P loops between negative and positive values of polarization with the change in relative oxygen pressure, ρ , from 1 to 10^{-6} .

The features of $A(E, T)$ behavior depend on T and ρ more weakly than the features of $P(E, T)$. The A loop is absent only for $\rho < 10^{-4}$ and above 350–450 K, which indicates the transition to the FE-like AFI state due to

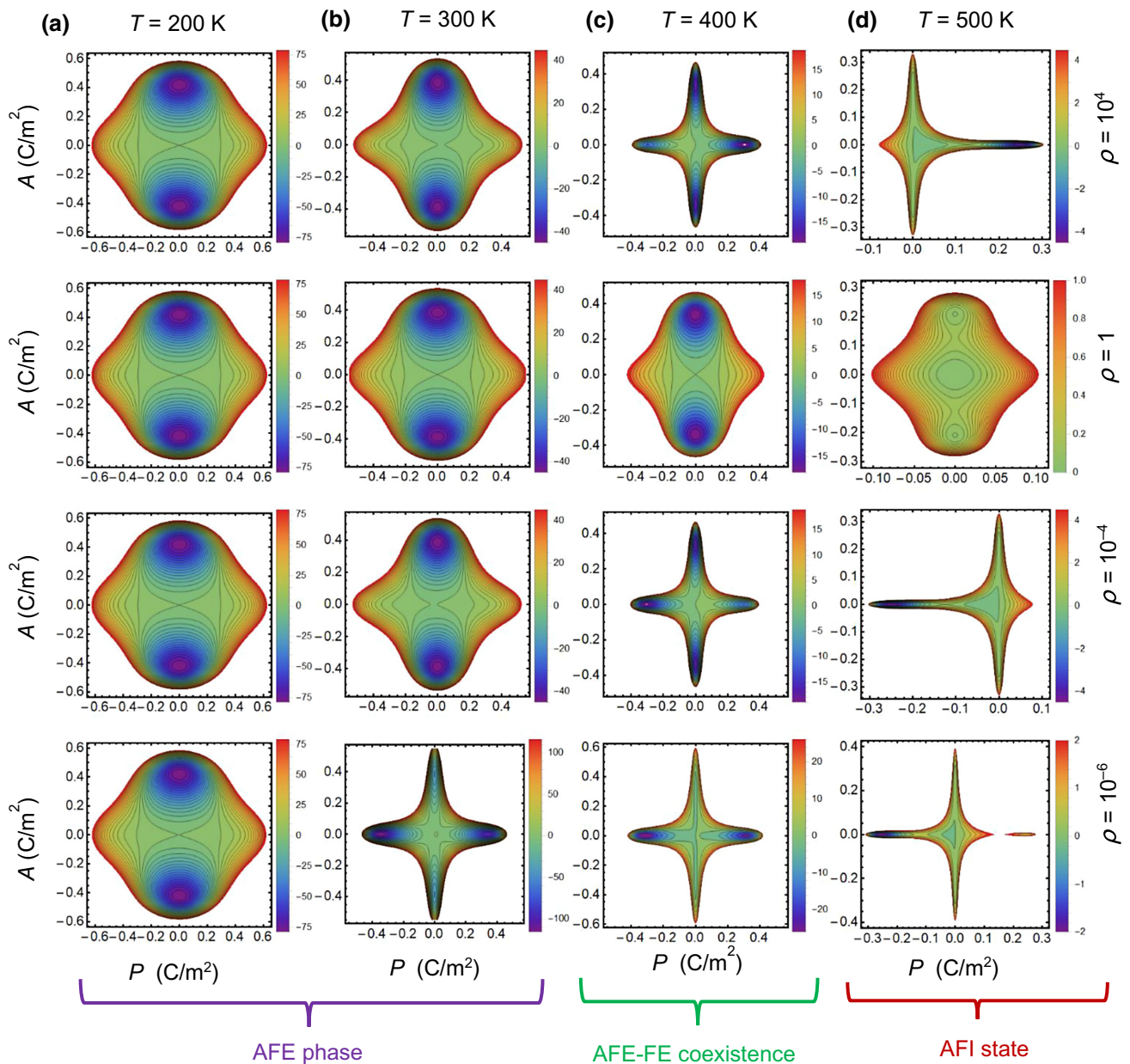


FIG. 3. Free energy as a function of polarization (P) and antipolarization (A) calculated for $T=200$ (a), 300 (b), 400 (c), and 500 K (d), and relative partial oxygen pressures $\rho = 10^4$, 1, 10^{-4} , and 10^{-6} ; values are listed for each column or row. Relative units are used for the energy color scale. External electric field is absent, $E = 0$. Thickness of AFE film, $h = 50$ nm; gap thickness, $\lambda = 2$ nm; and ion-formation energies, $\Delta G_1^{00} = \Delta G_2^{00} = 0.2$ eV.

the absence of “ionic support” from the AFE state. At lower partial oxygen pressures, the shape of the A loop is close to rectangular; its width and height depend on temperature and pressure. The A loop disappears at external fields larger than the critical value, E_c , since A no longer exists.

A decrease of A magnitude with increasing electric field E in the range of $E < E_c$ corresponds to the increase of P , and the $A(E)$ curves are almost symmetric with respect to the E axis, while the $P(E)$ curves acquire a more noticeable

asymmetry between positive and negative P values with a decrease of ρ from 1 to 10^{-6} .

$P(E)$ curves supplemented with red dotted vertical lines are virtually static double loops at $\rho = 1$ and become hysteresisless only at $T > 500$ K. The coercive field and the loop height decrease with temperature at $\rho = 1$ (as it should be). The double P loops transform into loops with a thin constriction in the vicinity of $E = 0$ as ρ decreases and the temperature increases. Then, the constriction significantly increases for $\rho = 10^{-4}$ and $T \geq 300$ K, and

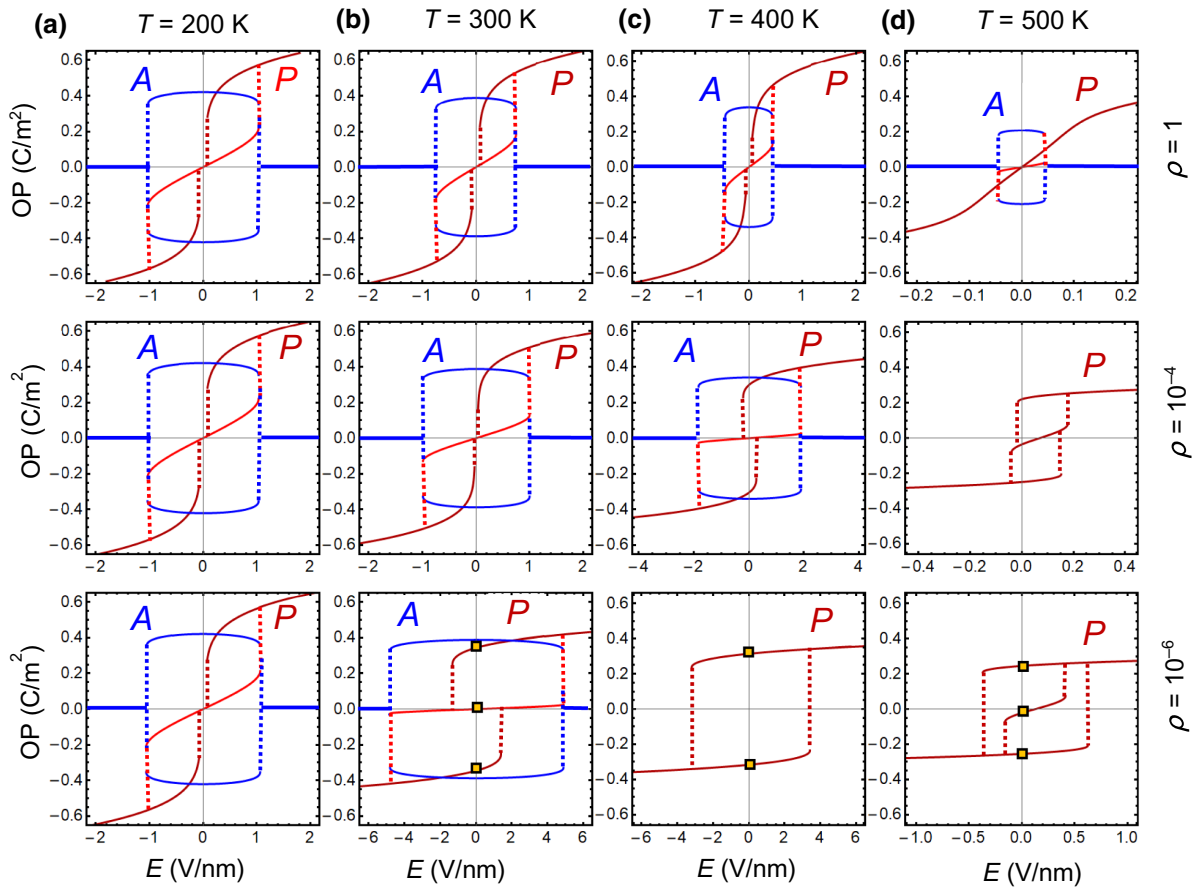


FIG. 4. Static dependences of order parameters (OPs) A (solid blue curves) and P (solid red and dark-red curves), on external electric field E calculated for $T = 200$ (a), 300 (b), 400 (c), and 500 K (d) and relative partial oxygen pressures $\rho = 1$, 10^{-4} , and 10^{-6} ; values are listed for each column or row. Dotted vertical lines show thermodynamic transitions between different polar and antipolar states; yellow rectangles mark two or three stable polarization states. External electric field is $E = (U/h)$. Other parameters are the same as those in Fig. 3.

eventually the static loop with a wide constriction transforms into a ferroelectriclike single loop for $\rho = 10^{-6}$ and $T \geq 400$ K. The FE-like single P loops correspond to the AFI state, because the surface ions support FE polarization and suppress the antipolar AFE order.

Notably, the $P(E)$ curves have no asymmetry for $\rho = 1$, since the built-in field, E_{SI} , is absent in this case. The $P(E)$ curves are slightly shifted to the right for $\rho < 1$, since E_{SI} is positive. The shift increases significantly as ρ decreases below 10^{-4} and T increases above 400 K. The P curves for $\rho = 10^{-4}$ are shifted to the left, since E_{SI} is negative in this case, as shown in Fig. E1 within the Supplemental Material [35].

Polarization hysteresis loops, $P(E)$, calculated for dimensionless frequencies $w = 0.3 - 100$, temperatures $T = 200 - 500$ K, and relative oxygen pressures $\rho = 1 - 10^{-6}$ are shown in Fig. 5. As the relative pressure decreases from 1 to 10^{-4} and at relatively low frequencies, $w \leq 10$, the loop shape demonstrates a continuous transition from a double loop in the AFE phase to a single loop in the AFI

state, and then the loop disappears in the PE phase. Only a single loop exists at $\rho = 10^{-6}$ and $T \geq 300$ K, and it gradually degrades to a shifted hysteresisless PE curve with a temperature increase far above 600 K (not shown in the figure). The frequency increase ($w \geq 30$) transforms a double loop into a loop with constriction, and then it “opens” a single loop. Loop opening is a dynamic effect similar to the one shown in Figs. 2(h)–2(j). Both quasi-static ($w \leq 10$) and dynamic ($w \geq 30$) loops are slightly right-shifted at $\rho < 1$, and the shift is proportional to the built-in field, E_{SI} . The shift increases as ρ decreases below 10^{-4} and T increases above 400 K. The P curves for $\rho = 10^{-4}$, which are left-shifted (since E_{SI} is negative in this case), are shown in Fig. E2 within the Supplemental Material [35].

A typical phase diagram of a thin AFE film, depending on the temperature, T , and relative oxygen pressure, $\rho \leq 1$, is shown in Fig. 6(a) for $h = 50$ nm and in Fig. 6(b) for $h = 5$ nm. There is an AFE phase, an AFE phase coexisting with a weak FE phase, a FE-like AFI phase, and an electretlike PE phase. Figures 6(c)–(e) illustrate that

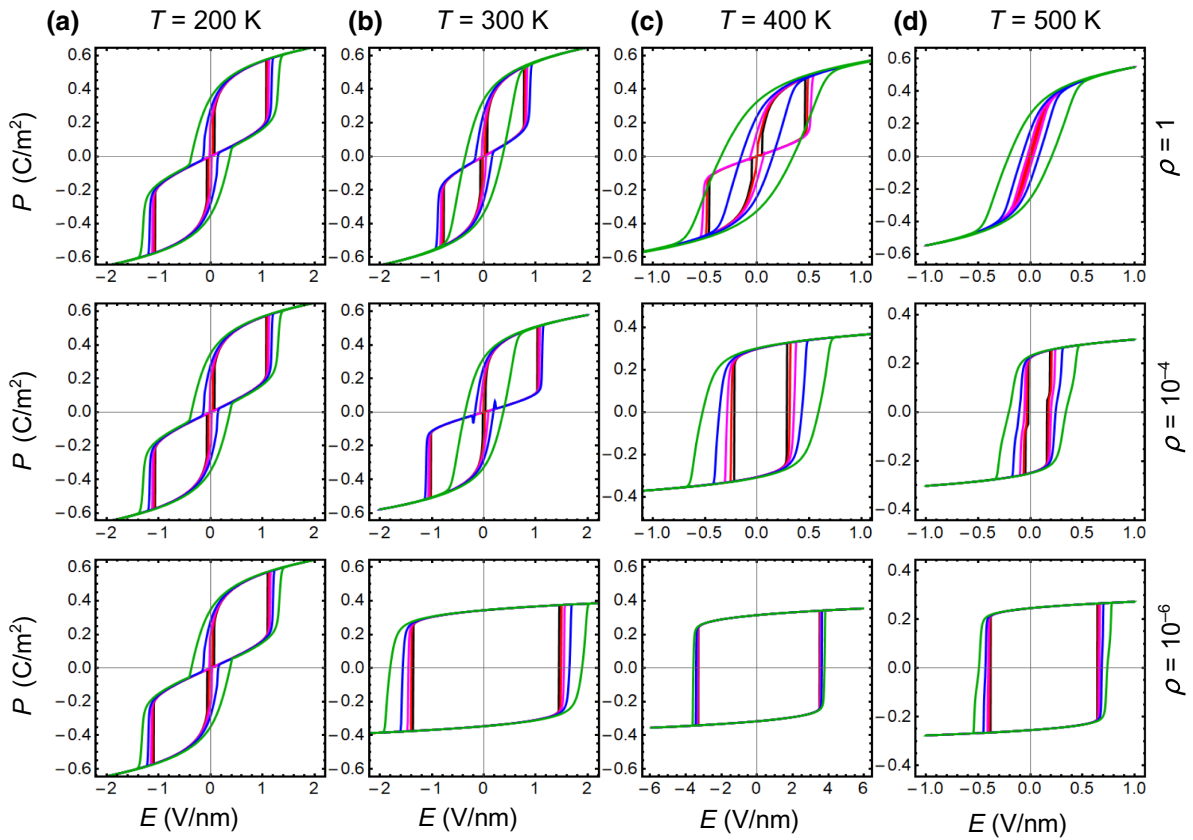


FIG. 5. Polarization hysteresis loops, $P(E)$, calculated for dimensionless frequencies $w = 0.3$ (black loops), 3 (red loops), 10 (magenta loops), 30 (blue loops), and 100 (green loops) at temperatures $T = 200$ (a), 300 (b), 400 (c), and 500 K (d), and relative partial oxygen pressures, $\rho = 1, 10^{-4}$, and 10^{-6} ; values are listed for each column or row. External electric field is $E = (U_0/h) \sin(\omega t)$ and $w = (\omega \Gamma_P / 2 |\alpha_p|)$. Other parameters are the same as those in Fig. 3.

the typical free-energy relief is AFE-FE, FE-like FEI, and electretlike PE phases, respectively. Figures 6(f)–(h) are typical hysteresis loops in these phases. The phase diagram plotted for relative pressures from 10^{-6} to 10^6 is shown in Fig. E3 within the Supplemental Material [35].

The wide light-blue AFE-FE coexistence region increases as h decreases [compare Figs 6(a) and 6(b)], but it is located at temperatures lower than 500 K (that is, slightly higher than $T_A \cong 490$ K) independent of the film thickness, because antipolarization is insensitive to the depolarization field. The relatively small light-green region of the AFI phase decreases significantly as h decreases [compare Figs. 6(a) and 6(b)], because polarization is very sensitive to the depolarization field, E_d , which is inversely proportional to the film thickness, $E_d \sim -\{\lambda P / [\epsilon_0 (\epsilon_d h + \lambda \epsilon_{33}^b)]\}$ [see Eq. (5c)]. The AFI phase corresponds to rather low relative oxygen pressures ($\rho \leq 2 \times 10^{-4}$ for $h = 50$ nm or $\rho \leq 10^{-5}$ for $h = 5$ nm), but exists over a relatively wide temperature range ($250 \text{ K} \leq T \leq 500 \text{ K}$ for $h = 50$ nm, or $310 \text{ K} \leq T \leq 475 \text{ K}$ for $h = 5$ nm). The boundary between the AFE-FE region and the AFI phase is close to a rounded corner. The boundary

between the AFE-FE, AFI, and PE phases (local inside a sand-colored region) is close to the vertical line at $T \cong 500$ K.

Notably, the phase set, namely, AFE, AFE-FE, FE-like AFE, and electretlike PE, shown in Fig. 6 differs from the analogous set (AFE, FEI, PE) shown in Figs. D1–D4 [35]. The difference originates from the difference in Landau expansion coefficients, $\beta_{a,p} > 0$ and $\gamma_{a,p} = 0$, for the 2-4 Landau expansion and $\beta_{a,p} < 0$ and $\gamma_{a,p} > 0$ for the 2-4-6 Landau expansion (compare material parameters from Table C1 with material parameters from Table D1 [35]).

C. The influence of surface ions on energy and information storage in thin AFE films

It is well known that energy loss is an area inside a hysteresis loop $P(E)$, further abbreviated as W_{loss} , and stored energy is equal to an area above the loop (in other words, the area between the loop and P axis), further abbreviated as W_{store} . Nonvolatile information storage requires high remanent polarization and a not very small coercive field, and thus, the optimal W_{loss} . If the loop is absent and $P \cong$

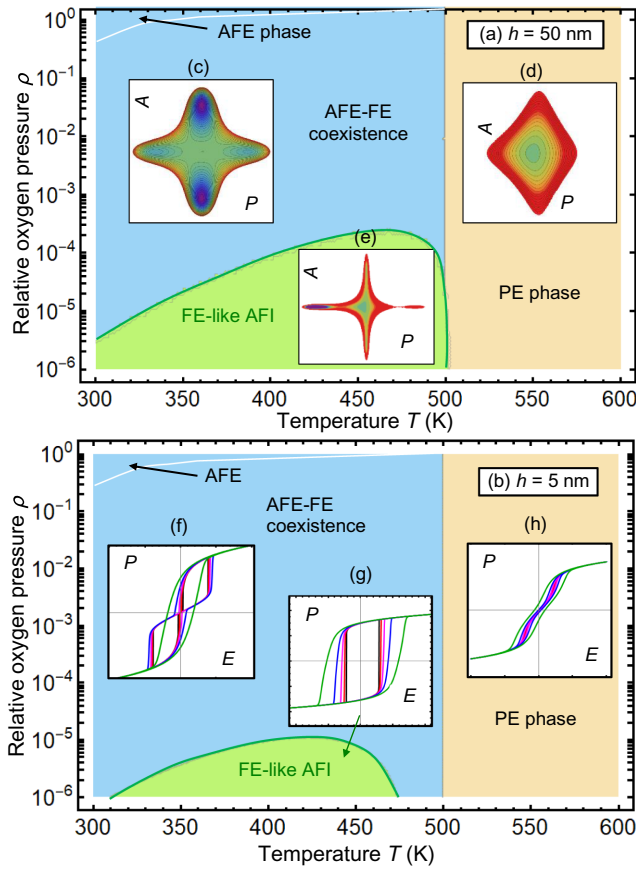


FIG. 6. Typical phase diagrams of thin AFE films with thicknesses $h = 50$ nm (a) and $h = 5$ nm (b), depending on temperature, T , and relative partial oxygen pressure, ρ . There is an AFE phase coexisting with a weak FE phase, a FE-like AFI phase, and an electretlike PE phase. Typical free-energy maps at $E = 0$ (b)–(d), and polarization hysteresis loops, $P(E)$ (e)–(g). Description of the insets is the same as those in Figs. 3 and 5. Other parameters are the same as those in Fig. 3.

χE , the loss is absent, and the stored energy is $(\chi/2)E^2$. However, nonvolatile information storage is impossible in this case.

For a single quasi-rectangular ferroelectric hysteresis loop with polarization saturation above the coercive field, the stored energy is small (zero in the limit of a rectangular loop), and the loop area is given by the approximate expression $W_{\text{loss}} = 2P_S(E_{c2} - E_{c1})$ [see Fig. 1(b)]. The expressions for the spontaneous polarization, P_S , and coercive fields, E_{ci} , in the case of the second-order phase transitions are given in Table I. The area of a double loop is given by approximate expression, $W_{\text{loss}} = \Delta P(E_{c3} - E_{c1}) + \Delta P(E_{c2} - E_{c4})$, and the stored energy is $W_{\text{store}} = (\varepsilon/2)(E_{c1}^2 + E_{c2}^2) + \Delta P(E_{c1} - E_{c2})$. For the case of polarization saturation above the critical field, a rough approximation, $(W_{\text{loss}}/W_{\text{store}}) \sim [(E_{c3} - E_{c4})/(E_{c1} - E_{c2})] - 1$, is valid. If all four coercive fields exist, we find that $(W_{\text{loss}}/W_{\text{store}}) \sim [1 - (\chi_R \alpha_a / 2\alpha_{pR} \beta_a)]^{-3/2} - 1$ for the AFE

film with second-order phase transitions [$\beta_{a,p} > 0$ and $\gamma_{a,p} = 0$ in Eq. (6)].

It follows from the above expressions that one needs a large steplike (or quasi-linear with a small slope) hysteresisless region (e.g., $P \cong \varepsilon E$, where ε is small) for maximal energy storage. Without this region, loop-shape optimization for energy storage in the space of parameters $\{\rho, T, h\}$ leads to a trivial result: no loop at all, i.e., the hysteresisless curve in the PE phase. The presence of the linear region adds an additional trapezoidal area above the $P(E)$ curve [or between the $P(E)$ loop and P axis], and energy storage also becomes favorable in the AFE phase [see Fig. 1(b)]. Since we show that oxygen deficiency (or excess) can transform a double AFE loop into a single FE-like one (compare loops in Fig. 5), the use of the AFI film for energy storage is not beneficial; at the same time, information storage in AFI films can possess several advantages. Let us discuss the question in more detail for the AFE film with first-order phase transitions [$\beta_{a,p} < 0$ and $\gamma_{a,p} > 0$ in Eq. (6)].

Figure 7(a) illustrates that the double-hysteresis loops with a pronounced linear region between the loops can only exist at room temperature in ultrathin AFE films ($h \leq 10$ nm) if the relative oxygen pressure does not deviate significantly from normal conditions, $10^{-3} \leq \rho \leq 1$. At the same time, the linear region is almost absent for thicker films [see Fig. 7(b)]. At temperatures above T_A , an ultrathin film becomes either paraelectric for $\rho \cong 1$ or electretlike for $\rho \ll 1$, and corresponding hysteresisless $P(E)$ curves cannot be used for information storage, because their area is zero [see Fig. 7(c)], while double-hysteresis loops with a very small loop area (and, consequently, very small losses) can exist in a thicker film for $\rho \leq 10^{-4}$ and $T \geq T_A$ [see Fig. 7(d)]. Similar plots for film thicknesses of 5, 10, 20, and 50 nm are shown in Fig. E4 within the Supplemental Material [35].

Hence, we can conclude that energy storage at room temperature is only viable in ultrathin AFE films ($h \leq 10$ nm) when the relative oxygen pressure does not deviate significantly from normal conditions, $10^{-3} \leq \rho \leq 1$. Also, energy storage is favorable in thicker films ($50 \leq h \leq 100$ nm) at elevated temperatures slightly above T_A and relative pressures of $\rho \leq 10^{-4}$.

To quantify the conclusion, we calculate the dependence of the hysteresis loop shape, W_{loss} , and W_{store} on the relative pressure, temperature, and film thickness, and these results are shown in Figs. E5–E7 within the Supplemental Material [35]. After analyzing the results shown in Fig. 7 and Figs. E5–E7 [35], we compose a schematic diagram of the correlation between the loop shape, energy loss, and stored energy, depending on the relative pressure, ρ , and temperature, T ; it is shown in Fig. 8(a). Color maps of W_{store} and W_{loss} are shown in Figs. 8(b) and 8(c), respectively. The hysteresis-loop map (black curves) is superimposed on the W_{store} and W_{loss} color maps. As expected, the loop shape,

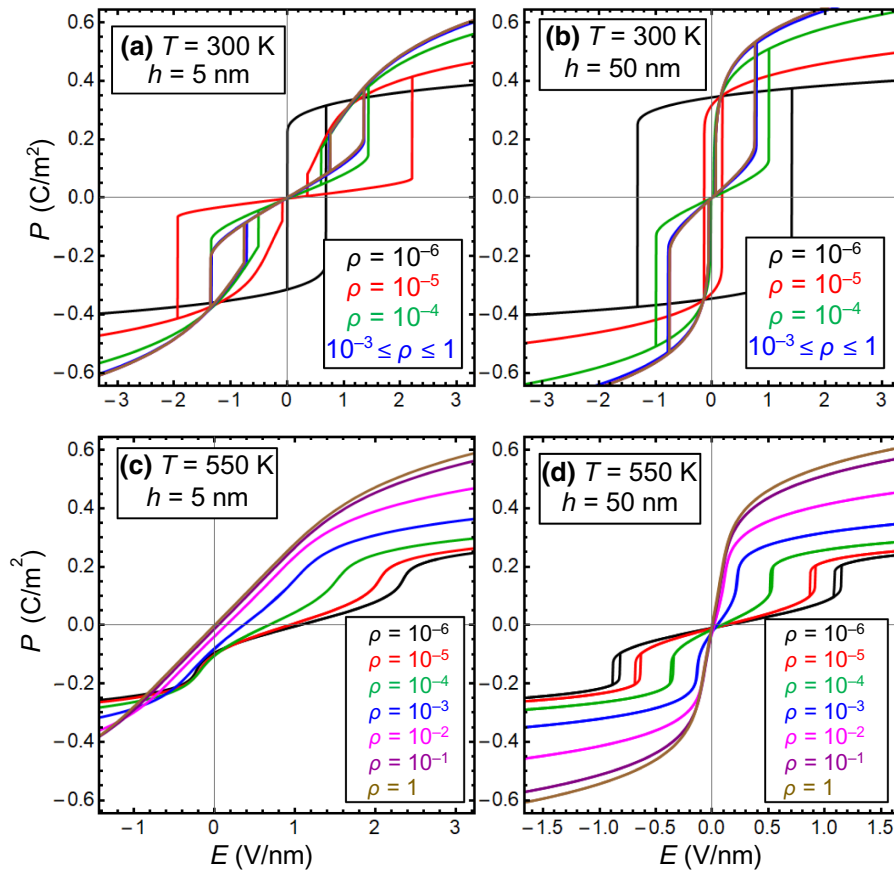


FIG. 7. Polarization field dependence, $P(E)$, calculated for a very low dimensionless frequency, $w = 10^{-3}$; $T = 300$ (a),(b) and 550 K (c),(d); relative partial oxygen pressure, $\rho = 10^{-6}$ (black curves), 10^{-5} (red curves), 10^{-4} (green curves), 10^{-3} (blue curves), 10^{-2} (magenta curves), 10^{-1} (purple curves), and 1 (brown curves). Film thickness, $h = 5$ (a),(b) and 50 nm (c),(d). External electric field is $E = (U_0/h) \sin(\omega t)$ and $w = (\omega \Gamma_p / 2 |\alpha_p|)$. Other parameters are the same as those in Fig. 3.

W_{store} , and W_{loss} definitely correlate with the efficiency of energy and information storage in the AFE films exposed to oxygen pressure.

From the diagram, we conclude that region I, of double loops with a pronounced linear region, is the most suitable for high-density energy storage and less suitable for volatile information storage, because the W_{loss} is high and the W_{store} is relatively small. Non-volatile information storage is impossible for this type of double loop, since the spontaneous polarization, P_S , is absent at zero and small voltages, $P_S(0) = 0$. Region I is the biggest: it corresponds to pressures of $10^{-3} \leq \rho \leq 1$ and temperatures of $T < T_A$, and the area of the region slowly decreases as ρ decreases and/or T increases.

Region II corresponds to double loops without a linear region. The loops are characterized by high losses, and thus, are neither suitable for nonvolatile information storage [since $P_S(0) = 0$ for the loops] nor for effective energy storage (since W_{loss} is small). However, these types of loops are ideally suited resistive-type (i.e., volatile) information storage, since SA is high for each minor loop. Region II has the shape of a curved stripe. This region corresponds to pressures of $10^{-3} \leq \rho \leq 1$ and temperatures of $T < T_A$; its area increases as ρ decreases, and it borders region I.

The narrowest region, III, contains single loops with a pronounced constriction, which are suitable for information storage that is mostly nonvolatile, but the loops are less suitable for energy storage, since W_{loss} is rather high and W_{store} is very small. The boundaries of this region are diffuse, and it is located at pressures of $10^{-6} \leq \rho \leq 10^{-3}$ and over wide temperature range of $T < 500 \text{ K}$.

Region IV contains FE-like single AFI loops without a pronounced constriction, which is suitable for nonvolatile information storage but unsuitable for energy storage. This region is a bit wider than the region of the AFI phase shown in Fig. 6. Region V, which is mostly the PE phase, is suitable for low-density energy storage in a definite sense, because the height of the polarization step is relatively small, but the W_{loss} is very small and the W_{store} is large [see green, black, and red curves in Fig. 7(d)].

V. DISCUSSION AND OUTLOOK

Using the phenomenological parameters of LGD thermodynamic potential, we explore the role of the surface-ion layer with a charge density proportional to the partial oxygen pressure on the dipole states, their reversal mechanisms, and the corresponding phase diagrams of AFE thin films using a Stephenson-Highland approach. The combined LGDSH approach allows us to delineate

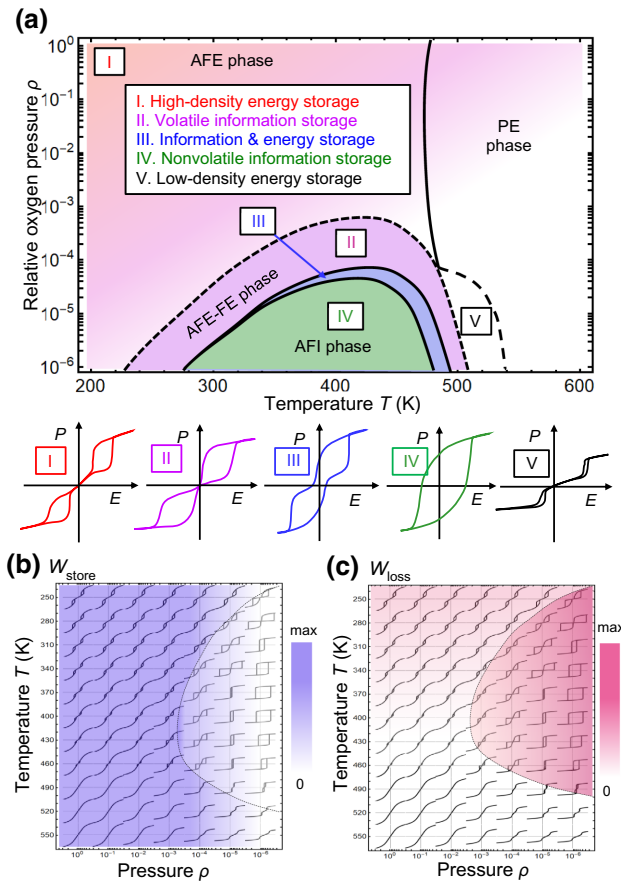


FIG. 8. (a) Schematic diagram relating loop shape, information, and energy-storage abilities to relative pressure, ρ , and temperature, T . Roman letters I–V indicate the five regions described in the text. Color maps of W_{store} (b) and W_{loss} (c) of the $P(E)$ dependences. Hysteresis loops (black curves) are superimposed on color maps. Film thickness, $h = 5$ nm. Other parameters are the same as those in Fig. 3.

the boundaries of the AFE, FE-like AFI, and electretlike PE states as a function of temperature, oxygen pressure, surface-ion formation energy and concentration, and film thickness. This approach also permits the characterization of the polarization and antipolarization dependence on the voltage applied to the antiferroelectric film, as well as analysis of the static and dynamic hysteresis loop features. Importantly, the LGDSH approach proposes an alternative model for the frequently observed ferroelectricity in AFE thin films [57] and provides a numerical model for energy storage in materials with an AFI state.

For applications, our modeling is able to select parameters that can tune the position where a transition to the FE-like AFI state happens and minimize (or maximize) the area of hysteresis loops. Also, our results are interesting for the implementation multibit nonvolatile random access memory (NRAM). As a matter of fact, a “single” hysteresis loop, $P(E)$, with two values of spontaneous polarization, $\pm P_S$, implements a “binary” bit in uniaxial

ferroelectrics. In the case of a thin film of multiaxial ferroelectric, the coexistence of several phases with different directions of the polarization vector and its magnitude is possible. Recently, Baudry *et al.* [58] predicted the existence of a multiwell free-energy relief in a thin strained PbTiO_3 film, with the possibility of transitions between wells under the action of an electric field. Depending on the misfit strain and temperature, two (c phase), three (aa phase), and four (r phase) stable phases with different spontaneous polarizations are possible, which implement 4-bit, 3-bit, or “normal” 2-bit systems. However, the transition between multibits is possible only by changing the misfit strain, which is difficult to implement during film exploitation in a memory cell. The considered AFI system, “antiferroelectric film + surface-ion layer,” allows switching between two or three stable polarization states (see 2 or 3 yellow rectangles on the static loops in Fig. 4), which can implement ternary bits, and the transition of the nonvolatile memory cell to a 3-bit system is possible by changing the partial oxygen pressure, which is easier from a technological point of view and possible during cell operation.

However, in this work, we do not consider phases with several orientations of polarization and antipolarization, leaving this for future studies, realizing that multiaxiality can lead to the appearance of additional stable phases of free energy and increasing the number of multibits in the AFI-based NRAM.

To summarize, our approach results in an overview of the phase diagrams of thin AFE films covered by a surface-ion layer and explores the specifics of polarization reversal and antipolar ordering in the system, to quantify film applications for energy and information storage, such as AFI NRAM. On the other hand, many important questions, such as the polarization multiaxiality, finite-size effect, and its influence on domain formation and evolution, remain for further studies.

ACKNOWLEDGMENTS

The authors are very grateful to Dr. Bobby Sampter and the referees for very useful remarks and stimulating discussions. This effort is based upon work supported by the U.S. Department of Energy, Office of Science, Office of Basic Energy Sciences Energy Frontier Research Centers program under Award No. DE-SC0021118 (S.V.K.) and performed at the Oak Ridge National Laboratory’s Center for Nanophase Materials Sciences (CNMS), a U.S. Department of Energy, Office of Science User Facility. Work by A.N.M. and N.V.M. is supported by the National Academy of Sciences of Ukraine. This work is supported, in part (A.B.), by the U.S. Department of Energy, Office of Science, Office of Basic Energy Sciences, as part of the Energy Frontier Research Centers program, Center for the Science of Synthesis Across Scales (CSSAS), under

Award No. DE-SC0019288, located at the University of Washington and performed at Oak Ridge National Laboratory's Center for Nanophase Materials Sciences (CNMS), a U.S. Department of Energy, Office of Science User Facility. Work by A.N.M is supported by the National Research Foundation of Ukraine (Grant No. Φ 81/41481). This work has been partially supported by U.S. DOE Grant No. DE-FG02-13ER41967. ORNL is managed by UT-Battelle, LLC, under Contract No. DE-AC05-00OR22725 for the U.S. Department of Energy.

S.V.K. and A.N.M. generated the research idea. A.N.M. proposed the theoretical model, derived analytical results, and interpreted numerical results obtained by E.A.E. A.B. used the Gaussian process model for rapid exploration and prediction of phase diagrams. A.N.M. and S.V.K. wrote the manuscript draft. Then S.V.K. and N.V.M. worked on the results discussion and manuscript improvement.

-
- [1] A. K. Tagantsev, L. E. Cross, and J. Fousek, *Domains in Ferroic Crystals and Thin Films* (Springer, New York, 2010).
- [2] A. M. Bratkovsky and A. P. Levanyuk, Continuous theory of ferroelectric states in ultrathin films with real electrodes, *J. Comput. Theor. Nanosci.* **6**, 465 (2009).
- [3] A. M. Bratkovsky and A. P. Levanyuk, Effects of anisotropic elasticity in the problem of domain formation and stability of monodomain state in ferroelectric films, *Phys. Rev. B* **84**, 045401 (2011).
- [4] S. V. Kalinin and D. A. Bonnell, Screening phenomena on oxide surfaces and its implications for local electrostatic and transport measurements, *Nano Lett.* **4**, 555 (2004).
- [5] S. Jesse, A. P. Baddorf, and S. V. Kalinin, Switching spectroscopy piezoresponse force microscopy of ferroelectric materials, *Appl. Phys. Lett.* **88**, 062908 (2006).
- [6] A. N. Morozovska, S. V. Svechnikov, E. A. Eliseev, S. Jesse, B. J. Rodriguez, and S. V. Kalinin, Piezoresponse force spectroscopy of ferroelectric-semiconductor materials, *J. Appl. Phys.* **102**, 114108 (2007).
- [7] A. V. Ievlev, S. Jesse, A. N. Morozovska, E. Strelcov, E. A. Eliseev, Y. V. Pershin, A. Kumar, V. Y. Shur, and S. V. Kalinin, Intermittency, quasiperiodicity and chaos in probe-induced ferroelectric domain switching, *Nat. Phys.* **10**, 59 (2013).
- [8] A. V. Ievlev, A. N. Morozovska, V. Ya. Shur, and S. V. Kalinin, Humidity effects on tip-induced polarization switching in lithium niobate, *Appl. Phys. Lett.* **104**, 092908 (2014).
- [9] E. V. Chensky and V. V. Tarasenko, Theory of phase transitions to inhomogeneous states in finite ferroelectrics in an external electric field, *Sov. Phys. JETP* **56**, 618 (1982) [*Zh. Eksp. Teor. Fiz.* **83**, 1089 (1982)].
- [10] M. Stengel and N. A. Spaldin, Origin of the dielectric dead layer in nanoscale capacitors, *Nature* **443**, 679 (2006).
- [11] N. Domingo, I. Gaponenko, K. Cordero-Edwards, Nicolas Stucki, V. Pérez-Dieste, C. Escudero, E. Pach, A. Verdaguier, and P. Paruch, Surface charged species and electrochemistry of ferroelectric thin films, *Nanoscale* **11**, 17920 (2019).
- [12] J. E. Spanier, A. M. Kolpak, J. J. Urban, I. Grinberg, L. Ouyang, W. S. Yun, A. M. Rappe, and H. Park, Ferroelectric phase transition in individual single-crystalline BaTiO₃ nanowires, *Nano Lett.* **6**, 735 (2006).
- [13] R. V. Wang, D. D. Fong, F. Jiang, M. J. Highland, P. H. Fuoss, C. Tompson, A. M. Kolpak, J. A. Eastman, S. K. Streiffer, A. M. Rappe, and G. B. Stephenson, Reversible Chemical Switching of a Ferroelectric Film, *Phys. Rev. Lett.* **102**, 047601 (2009).
- [14] D. D. Fong, A. M. Kolpak, J. A. Eastman, S. K. Streiffer, P. H. Fuoss, G. B. Stephenson, C. Thompson, D. M. Kim, K. J. Choi, C. B. Eom, I. Grinberg, and A. M. Rappe, Stabilization of Monodomain Polarization in Ultrathin PbTiO₃ Films, *Phys. Rev. Lett.* **96**, 127601 (2006).
- [15] M. J. Highland, T. T. Fister, M.-I. Richard, D. D. Fong, P. H. Fuoss, C. Thompson, J. A. Eastman, S. K. Streiffer, and G. B. Stephenson, Polarization Switching Without Domain Formation at the Intrinsic Coercive Field in Ultrathin Ferroelectric PbTiO₃, *Phys. Rev. Lett.* **105**, 167601 (2010).
- [16] J. D. Baniecki, J. S. Cross, M. Tsukada, and J. Watanabe, H₂O vapor-induced leakage degradation of Pb(Zr, Ti)O₃ thin-film capacitors with Pt and IrO₂ electrodes, *Appl. Phys. Lett.* **81**, 3837 (2002).
- [17] Y. Gu, K. Xu, C. Song, X. Zhong, H. Zhang, H. Mao, M. S. Saleem, J. Sun, W. Liu, Z. Zhang, F. Pan, and J. Zhu, Oxygen-valve formed in cobaltite-based heterostructures by ionic liquid and ferroelectric dual-gating, *ACS Appl. Mater. Interfaces* **11**, 19584 (2019).
- [18] N. C. Bristowe, M. Stengel, P. B. Littlewood, J. M. Pruneda, and E. Artacho, Electrochemical ferroelectric switching: Origin of polarization reversal in ultrathin films, *Phys. Rev. B* **85**, 024106 (2012).
- [19] S. V. Kalinin and D. A. Bonnell, Effect of phase transition on the surface potential of the BaTiO₃ (100) surface by variable temperature scanning surface potential microscopy, *J. Appl. Phys.* **87**, 3950 (2000).
- [20] S. V. Kalinin, C. Y. Johnson, and D. A. Bonnell, Domain polarity and temperature induced potential inversion on the BaTiO₃(100) surface, *J. Appl. Phys.* **91**, 3816 (2002).
- [21] S. Bühlmann, E. Colla, and P. Muralt, Polarization reversal due to charge injection in ferroelectric films, *Phys. Rev. B* **72**, 214120 (2005).
- [22] Y. Kim, S. Bühlmann, S. Hong, S. H. Kim, and K. No, Injection charge assisted polarization reversal in ferroelectric thin films, *Appl. Phys. Lett.* **90**, 072910 (2007).
- [23] Y. Kim, J. Kim, S. Bühlmann, S. Hong, Y. K. Kim, S.-H. Kim, and K. No, Screen charge transfer by grounded tip on ferroelectric surfaces, *Phys. Status Solidi (RRL)* **2**, 74 (2008).
- [24] A. V. Ievlev, A. N. Morozovska, E. A. Eliseev, V. Y. Shur, and S. V. Kalinin, Ionic field effect and memristive phenomena in single-point ferroelectric domain switching, *Nat. Commun.* **5**, 4545 (2014).
- [25] G. B. Stephenson and M. J. Highland, Equilibrium and stability of polarization in ultrathin ferroelectric films with

- ionic surface compensation, *Phys. Rev. B* **84**, 064107 (2011).
- [26] H. Lu, C.-W. Bark, D. E. De Los Ojos, J. Alcalá, C.-B. Eom, G. Catalan, and A. Gruverman, Mechanical writing of ferroelectric polarization, *Science* **336**, 59 (2012).
- [27] C. W. Bark, P. Sharma, Y. Wang, S. H. Baek, S. Lee, S. Ryu, C. M. Folkman, T. R. Paudel, A. Kumar, S. V. Kalinin, A. Sokolov, E. Y. Tsymbal, M. S. Rzchowski, A. Gruverman, and C. B. Eom, Switchable induced polarization in $\text{LaAlO}_3/\text{SrTiO}_3$ heterostructures, *Nano Lett.* **12**, 1765 (2012).
- [28] Y. Cao, A. N. Morozovska, and S. V. Kalinin, Pressure-induced switching in ferroelectrics: Phase-field modeling, electrochemistry, flexoelectric effect, and bulk vacancy dynamics, *Phys. Rev. B* **96**, 184109 (2017).
- [29] M. J. Highland, T. T. Fister, D. D. Fong, P. H. Fuoss, C. Thompson, J. A. Eastman, S. K. Streiffer, and G. B. Stephenson, Equilibrium Polarization of Ultrathin PbTiO_3 with Surface Compensation Controlled by Oxygen Partial Pressure, *Phys. Rev. Lett.* **107**, 187602 (2011).
- [30] S. M. Yang, A. N. Morozovska, R. Kumar, E. A. Eliseev, Y. Cao, L. Mazet, N. Balke, S. Jesse, R. Vasudevan, C. Dubourdieu, and S. V. Kalinin, Mixed electrochemical-ferroelectric states in nanoscale ferroelectrics, *Nat. Phys.* **13**, 812 (2017).
- [31] A. N. Morozovska, E. A. Eliseev, N. V. Morozovsky, and S. V. Kalinin, Ferroionic states in ferroelectric thin films, *Phys. Rev. B* **95**, 195413 (2017).
- [32] A. N. Morozovska, E. A. Eliseev, N. V. Morozovsky, and S. V. Kalinin, Piezoresponse of ferroelectric films in ferroionic states: Time and voltage dynamics, *Appl. Phys. Lett.* **110**, 182907 (2017).
- [33] S. V. Kalinin, Y. Kim, D. D. Fong, and A. N. Morozovska, Surface screening mechanisms in ferroelectric thin films and its effect on polarization dynamics and domain structures, *Rep. Prog. Phys.* **81**, 036502 (2018).
- [34] A. N. Morozovska, E. A. Eliseev, A. I. Kurchak, N. V. Morozovsky, R. K. Vasudevan, M. V. Strikha, and S. V. Kalinin, Effect of surface ionic screening on polarization reversal scenario in ferroelectric thin films: Crossover from ferroionic to antiferroionic states, *Phys. Rev. B* **96**, 245405 (2017).
- [35] See the Supplemental Material at <http://link.aps.org/supplemental/10.1103/PhysRevApplied.16.044053> for calculation details in Appendices A–E, a Python notebook (also available at https://colab.research.google.com/drive/ljKbf2Yo5Y_ezmHaadjTB6qtxXYVfzg9T), and a MATHEMATICA 12.2 @Wolfram Research (<https://www.wolfram.com/mathematica>) notebook (also available at <https://notebookarchive.org/2021-06-bislk1z>).
- [36] A. K. Tagantsev and G. Gerra, Interface-induced phenomena in polarization response of ferroelectric thin films, *J. Appl. Phys.* **100**, 051607 (2006).
- [37] R. Blinc and B. Zeks, *Soft Mode in Ferroelectrics and Antiferroelectrics* (North-Holland Publishing Company, Amsterdam, Oxford, 1974).
- [38] R. W. Whatmore and A. M. Glazer, Structural phase transitions in lead zirconate, *J. Phys. C: Solid State Phys.* **12**, 1505 (1979).
- [39] M. J. Haun, T. J. Harvin, M. T. Lanagan, Z. Q. Zhuang, S. J. Jang, and L. E. Cross, Thermodynamic theory of PbZrO_3 , *J. Appl. Phys.* **65**, 3173 (1989).
- [40] M. J. Haun, Z. Q. Zhuang, E. Furman, S. J. Jang, and L. E. Cross, Thermodynamic theory of the lead zirconate-titanate solid solution system, Part III: Curie constant and sixth-order polarization interaction dielectric stiffness coefficients, *Ferroelectrics* **99**, 45 (1989).
- [41] K. M. Rabe, in *Functional Metal Oxides*, edited by Satishchandra Balkrishna Ogale, T. Venky Venkatesan, and Mark Blamire (John Wiley & Sons, Weinheim, 2013), pp.221–244.
- [42] A. K. Tagantsev, K. Vaideeswaran, S. B. Vakhrushev, A. V. Filimonov, R. G. Burkovsky, A. Shaganov, D. Andronikova, A. I. Rudskoy, A. Q. R. Baron, H. Uchiyama, D. Chernyshov, A. Bosak, Z. Ujma, K. Roleder, A. Majchrowski, J.-H. Ko, and N. Setter, The origin of antiferroelectricity in PbZrO_3 , *Nat. Commun.* **4**, 2229 (2013).
- [43] J. Hlinka, T. Ostapchuk, E. Buixaderas, C. Kadlec, P. Kuzel, I. Gregora, J. Kroupa, M. Savinov, A. Klic, J. Dráhokoupil, I. Etxebarria, and J. Dec, Multiple Soft-Mode Vibrations of Lead Zirconate, *Phys. Rev. Lett.* **112**, 197601 (2014).
- [44] N. A. Pertsev, A. G. Zembilgotov, and A. K. Tagantsev, Effect of Mechanical Boundary Conditions on Phase Diagrams of Epitaxial Ferroelectric Thin Films, *Phys. Rev. Lett.* **80**, 1988 (1998).
- [45] R. Kretschmer and K. Binder, Surface effects on phase transitions in ferroelectrics and dipolar magnets, *Phys. Rev. B* **20**, 1065 (1979).
- [46] C.-L. Jia, V. Nagarajan, Jia-Q. He, L. Houben, T. Zhao, Ramamoorthy Ramesh, K. Urban, and R. Waser, Unit-cell scale mapping of ferroelectricity and tetragonality in epitaxial ultrathin ferroelectric films, *Nat. Mat.* **6**, 64 (2007).
- [47] A. K. Tagantsev, G. Gerra, and N. Setter, Short-range and long-range contributions to the size effect in metal-ferroelectric-metal heterostructures, *Phys. Rev. B* **77**, 174111 (2008).
- [48] K. Y. Foo and B. H. Hameed, Insights into the modeling of adsorption isotherm systems, *Chem. Eng. J.* **156**, 2 (2010).
- [49] A. I. Kurchak, A. N. Morozovska, S. V. Kalinin, and M. V. Strikha, Nontrivial temperature behavior of the carriers concentration in the nano-structure “graphene channel - ferroelectric substrate with domain walls, *Acta Mater.* **155**, 302 (2018).
- [50] Y. Cao and S. V. Kalinin, Phase-field modeling of chemical control of polarization stability and switching dynamics in ferroelectric thin films, *Phys. Rev. B* **94**, 235444 (2016).
- [51] B. D. Vujanovic and S. E. Jones, *Variational Methods in Nonconservative Phenomena* (Academic Press, San Diego, 1989).
- [52] E. Savaguchi and T. Kittaka, Antiferroelectricity and ferroelectricity in lead zirconate, *J. Phys. Soc. Japan* **7**, 336 (1952).
- [53] E. Savaguchi, Ferroelectricity versus antiferroelectricity in the solid solutions of PbZrO_3 and PbTiO_3 , *J. Phys. Soc. Japan* **8**, 615 (1953).

- [54] R. H. Dungan, H. M. Barnett, and A. H. Stark, Phase relations and electrical parameters in the ferroelectric-antiferroelectric region of the system $\text{PbZrO}_3\text{-PbTiO}_3\text{-PbNbO}_2\text{O}_6$ ”, *J. Am. Ceram. Soc.* **45**, 382 (1962).
- [55] P. Dufour, T. Maroutian, A. Chanthbouala, C. Jacquemont, F. Godel, L. Yedra, M. Otonicar, N. Guiblin, M. Bibes, B. Dkhil, S. Fusil, and V. Garcia, *Electric-field and Temperature Induced Phase Transitions in Antiferroelectric Thin Films of PbZrO_3* (ISAF, 2021). https://epapers.org/isaf2021/paper_id=3520
- [56] A. S. Mischenko, Qi Zhang, J. F. Scott, R. W. Whatmore, and N. D. Mathur, Giant electrocaloric effect in thin-film $\text{PbZr}_{0.95}\text{Ti}_{0.05}\text{O}_3$, *Science* **311**, 1270 (2006).
- [57] S. Chattopadhyay, P. Ayyub, V. R. Palkar, M. S. Multani, S. P. Pai, S. C. Pai, S. C. Purandare, and R. Pinto, Dielectric properties of oriented thin films of on Si produced by pulsed laser ablation, *J. Appl. Phys.* **83**, 7808 (1998).
- [58] L. Baudry, I. Lukyanchuk, and V. M. Vinokur, Ferroelectric symmetry-protected multibit memory cell, *Sci. Rep.* **7**, 42196 (2017).